HRTEM study of Co7W6 and its typical defect structure

Carvalho, P.A.; Haarsma, H.S.D.; Kooi, B.J.; Bronsveld, P.M.; Hosson, J.Th.M. De

Published in:
Acta Materialia

DOI:
10.1016/S1359-6454(00)00064-1

Publication date:
2000

PERGAMON

Acta mater. 48 (2000) 2703–2712

Acta MATERIALIA

www.elsevier.com/locate/actamat

HRTEM STUDY OF Co_7W_6 AND ITS TYPICAL DEFECT STRUCTURE

P. A. CARVALHO, H. S. D. HAARSMA, B. J. KOOI, P. M. BRONSVELD and J. TH. M. DE HOSSON†

Department of Applied Physics, Materials Science Centre, Netherlands Institute of Metals Research, University of Groningen, Nijenborgh 4, 9747 AG Groningen, The Netherlands

(Received 1 December 1999; accepted 19 January 2000)

Abstract—The tetrahedrally close-packed structure of Co_7W_6 (μ-phase) was studied by HRTEM. A massive presence of random sub-unit cell twins was detected. These planar defects were characterized in detail and the twinning probability at potential mirror planes was established. High-precision image simulation of the bulk structure and defect region was performed, using a simulated evolution optimization strategy to refine the imaging conditions. *Ab initio* calculations were carried out in order to determine the energy involved in twinning, as well as the distortion induced in the structure. © *2000 Acta Metallurgica Inc. Published by Elsevier Science Ltd. All rights reserved.*

Keywords: Intermetallic compounds; Microstructure; Transmission electron microscopy (TEM); Image analysis; *Ab initio* calculations

1. INTRODUCTION

In this work the Co_7W_6 version of the so-called μ-phase was studied. Planar defects present, identified as random sub-unit cell twins, were thoroughly characterized. The bulk structure and defect regions were imaged using a high-resolution TEM JEOL 4000EX/II with 0.165 nm of point-to-point resolution. The presence of dynamical diffraction effects and the non-linear image formation with severe lens aberrations makes it necessary in HRTEM to relate object and image by extensive calculations [1]. This is particularly crucial for complex structures, where coincidence between atomic column positions and sites of contrast extrema does not always exist and where the unit cell can only be partially resolved. Since a direct interpretation was not possible, the analysis of the μ-phase images was treated as a high-dimensional numerical optimization problem, aimed at an efficient retrieval of approximated imaging parameters. *Ab initio* calculations were carried out in order to determine the energy involved in twinning, as well as the distortion induced in the structure. The results obtained enabled the randomness of the twinning process to be characterized.

Precipitates of μ-phase are common in superalloys with a high content of Mo or W. In the Co–W system, this intermetallic compound exists with a limited solid solubility around a Co_7W_6 stoichiometry, the composition extending from 43.3 to 48.5 at.% W [2]. The crystal structure, first determined by Magneli and Westgren [3] and later refined for the isotypic Co_7Mo_6 by Forsyth and D'Alte da Veiga [4], belongs to the $R\bar{3}m$ space group. The lattice parameters in the hexagonal system range from 0.472 to 0.475 nm for a and 2.548 to 2.567 nm for c [3].

The μ-phase is part of a group of intermetallic compounds with complex crystal structures, called tetrahedrally close-packed structures, which exist in many systems of binary and ternary alloys. Andersson [5] showed that such structures could be derived from the relatively simple β-tungsten structure using crystallographic operations such as translation, rotation and reflection, and intergrowth. In particular, the μ-phase can be described as an intergrowth of tetrahedrally close-packed sheets with the Zr_4Al_3 and $MgCu_2$ type of structures. The sheets of both these structures being stacked alternatively and parallel to the basal plane. Structural defects, related to mistakes in the operations mentioned above, have since long been observed in tetrahedrally close-packed compounds, like the σ-phase (in the Fe–Mo [6] and Fe–Cr [7] systems) and the M- and P-phases (in the Fe–Mo [6, 8] and Mo–Co–Si [8, 9] systems). Twins and other planar defects which may be explained by mistakes in the alternat-

† To whom all correspondence should be addressed.

PII: S1359-6454(00)00064-1

ing intergrowth of the Zr_4Al_3 and $MgCu_2$ sheets have in turn been observed in the Fe_7W_6 [10], Fe_7Mo_6 [6, 8], and Co_7Mo_6 [11, 12] versions of the μ-phase. However, a quantitative characterization of the defect structures was not performed in this earlier work. Furthermore, to our knowledge, the Co_7W_6 version of the μ-phase has never been thoroughly investigated. In the present work quantitative HRTEM image analysis and *ab initio* calculations of the typical defect structure present in Co_7W_6 were carried out.

2. EXPERIMENTAL DETAILS AND SIMULATION METHODS

2.1. Materials, instruments and experimental procedures

A Co–W alloy containing 20 at.% of W was processed in an arc furnace, where the constituents (with 99.99 wt% of nominal purity) were melted together on a water-cooled copper bed under a protective argon atmosphere. TEM samples were prepared by slicing and grinding 3 mm discs down to 150 μm in thickness. Subsequent thinning until perforation was carried out either by ion-milling or by jet polishing with a solution of methanol and sulfuric acid. A JEOL 4000 EX/II microscope, operating at 400 kV, was used in the HRTEM work. The microscope instrumental parameters can be found in Table 1.

2.2. Image simulation

High-resolution imaging conditions were retrieved with the Iterative Digital Image Matching (IDIM) package program [13], using a simulated evolution optimization algorithm. IDIM organizes a multidimensional parameter search based on image simulations performed by the EMS [14] multislice programs. The hexagonal cell used to simulate the bulk structure corresponded to a Co-rich μ-phase with lattice parameters $a = 0.472$ nm and $c = 2.548$ nm [3]. The defect supercell was constructed by the periodic continuation technique and contained two planar defects separated by 8.5 nm. Its (non-relaxed) dimensions were based on the bulk cell parameters. The film emulsion and the scanner used were shown to respond linearly in the selected exposure regime. Filtering was not applied to the digitized experimental images. The grey scale of the experimental images was adjusted to the full range of contrast. No absolute intensity information (taken from the specimen hole) was taken into account, meaning that the average intensity is non-interpretable. To properly match the experimental and simulated images, with respect to their relative position, reciprocal space alignment was carried out before comparison. The numerical agreement factor used was the cross-correlation factor (xcf), which is adequate for the current conditions [13]. The optimization parameters included defocus, thickness, beam tilt and crystal tilt. The parameter mutations were limited to wide upper and lower bounds keeping in mind realistic imaging conditions. The evolution runs were set to be interrupted by a fixed maximum number of 100 generations (each corresponding to 20 matching trials). Due to the complexity of the structure and the presence of heavy atoms, some non-reliability of the image simulations was anticipated. Hence, no attempt was made to improve the matching between simulated and experimental images by allowing atom displacements at the defect regions.

Table 1. JEOL 4000 EX/II characteristics

Operating voltage	400 kV
Objective aperture diameter	13.1/nm
Spherical aberration coefficient	0.97 ± 0.02 mm
Defocus spread	7.8 ± 1.4 mm
Beam semi-convergence angle	0.8 mrad
Point-to-point resolution	0.165 nm
Scherzer defocus	47 nm
Information limit	0.14 nm

2.3. Atomistic calculations

To evaluate the energy and distortion involved in twinning, the defect structure was computed from *ab initio* electronic structure calculations. The approach relies on solving the Schrödinger equation iteratively by constructing the crystalline potential and the wavefunction simultaneously in a consistent manner. This was performed with the CASTEP [15] software included in the CERIUS2 package [16]. The calculations were carried out using a gradient-corrected local-density approximation to the density-functional theory (with a cut-off energy of 360 eV). Non-local Kleinman–Bylander pseudopotentials [17] were used to represent the ion/core-electron interactions. Once more, due to periodicity restrictions, a supercell was generated containing two planar defects (26 atoms). The defect supercell has a hexagonal lattice with approximately the same dimensions as the μ-phase at the basal plane, but with two-thirds of the c-axis, and belongs to the $P6_3/mmc$ space group. The total energy and forces were calculated and the atomic positions were refined by minimizing the energy until the largest force on an atom was reduced to less than about 2×10^{-12} N. The same calculations were performed for a perfect primitive rhombohedral cell (13 atoms).

3. RESULTS AND DISCUSSION

3.1. Structure

Experimental [110] selected-area diffraction patterns (SADPs) of the Co_7W_6 phase can be seen in

Figs 1(a) and (b). Ion-milling was used as the thinning method in Fig. 1(a) whereas jet polishing was used in Fig. 1(b). Both experimental SADPs were obtained with a selected-area aperture sampling a region of about 0.9 μm in diameter. A simulated [110] diffraction pattern for the Co_7W_6 structure is presented in Fig. 1(c). The simulation was carried out with EMS [14] under dynamical conditions and using a perfect supercell of the μ-phase. A best match was obtained for a thickness of 7 nm. The μ-phase general reflections require $-h+k+l=3n$. Reflections corresponding to both obverse (o) and reverse (r) forms of the rhombohedral cell were systematically present in the experimental SADPs, with the basal plane being a mirror symmetry plane for the heavily streaked superimposed diffraction patterns [Figs 1(a) and (b)]. The random nature of twinning induced streaking along the c^*-axis only at $h-k=3n\pm1$ rows (referred to the basic rhombohedral structure in the hexagonal system). The residual streaking observed along $h-k=3n$ rows is due to double diffraction and could be removed by tilting. The diffuse ring and the splitting of the streak lines, which can be seen in Fig. 1(a), resulted from structural damage induced by the ion-milling operation and could not be observed in samples thinned by jet polishing [see Fig. 1(b)].

Figure 2 shows a many-beam experimental image of the Co_7W_6 phase, which was obtained with 10 mrad of deviation from axial [110] illumination by tilting the specimen around the [1$\bar{1}$0] axis. The twin domains parallel to (001) induced a strong contrast modulation due to the deliberate specimen tilt. Since the width of the twin domains is a multiple of $1/3c$, it is now clear that the extra spots in the diffraction patterns result from sub-unit cell twinning.

The sub-unit cell twins have their atomic structure explained in Fig. 3. The μ-phase can be described as an intergrowth of tetrahedrally close-packed sheets with the Zr_4Al_3 and $MgCu_2$ structures. The sheets of both these structures are stacked alternatively and parallel to the (001) plane, in accordance with a rhombohedral configuration (ABC stacking of the two-sheet layers performed with a 1/3[211] vector). The μ-phase exhibits a typical planar defect structure where the interfaces are pure mirror planes, with the middle plane of every Zr_4Al_3 sheet being a potential twin plane. In Fig. 3 a twin was generated by mirroring the lower half of the obverse cell onto the upper half. This operation resulted in the transformation of the obverse B and C layers (B_o and C_o) into reverse B and C layers (B_r and C_r). Owing to symmetry, for each layer there is an obverse and a reverse possibility of close-packed stacking, i.e. either B_o or a B_r can be stacked onto A_o, either C_r or A_o can be stacked onto B_r, either C_o or A_r can be stacked onto B_o and so forth. Since a mirror reflection at the middle plane of Zr_4Al_3 is a symmetry operation for this sheet, the building mistake occurs when a $MgCu_2$ sheet takes the wrong configuration from the two possible options. Consequently, the atomic arrangement at the planar defect is similar to the untwinned crystal configuration up to a distance of 0.42 nm. Sequences like $A_oB_rA_oB_r\ldots$ result, if twinning takes place at every possible mirror plane. This new structure has a hexagonal lattice with the basal dimensions of the μ-phase hexagonal cell (but two-thirds of its c-axis) and belongs to the $P6_3/mmc$

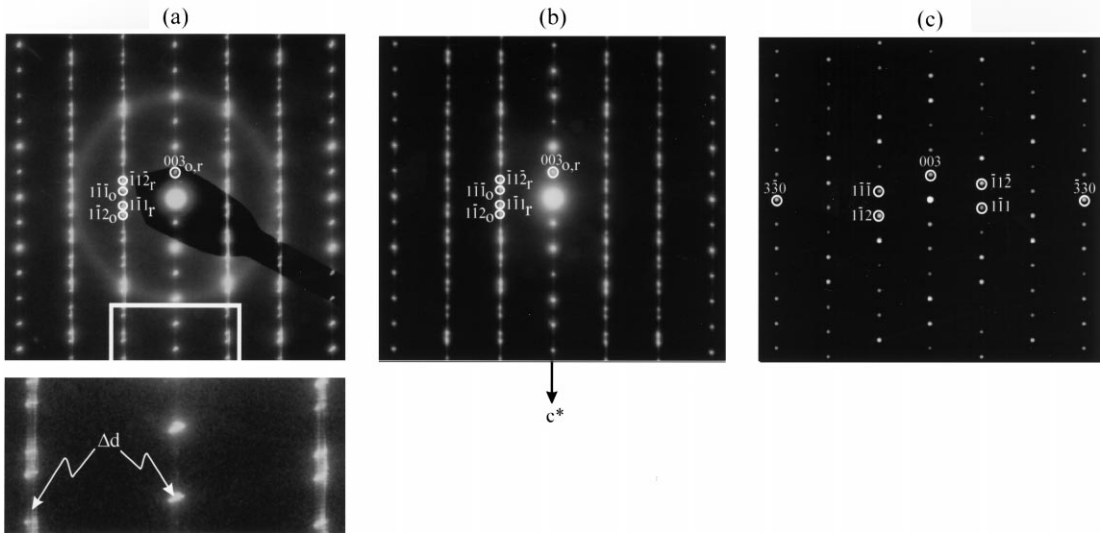

Fig. 1. Diffraction patterns of Co_7W_6 along the [110] zone axis of the hexagonal system: (a) ion-milled sample; (b) jet polished sample; (c) simulated. Streak splitting can clearly be seen in the magnification below (a). The expected positions for the basic obverse (o) and reverse (r) reflections are indicated in (a) and (b).

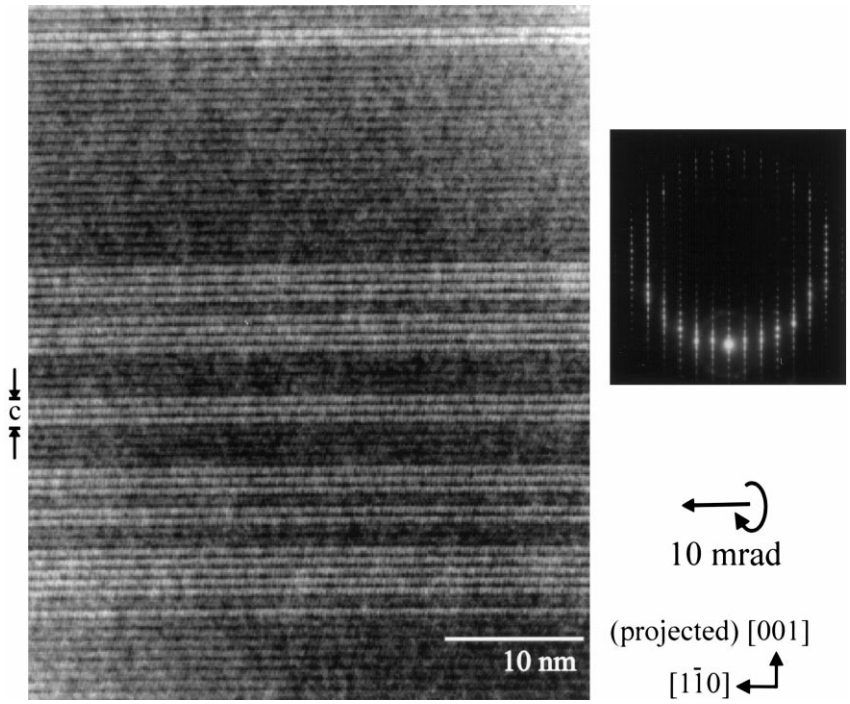

Fig. 2. Many-beam TEM picture of the Co_7W_6 phase and corresponding diffraction pattern, both obtained with a 10 mrad deviation from axial [110] illumination (hexagonal system). The contrast modulation along [0001] is related to random sub-unit cell twinning.

space group. Due to the high symmetry of the mirror operation, the new structures generated give rise to reflections at reciprocal lattice points coinciding with the common $h - k = 3n$ reflections of the basic rhombohedral forms. The structure corresponding to an $A_oB_rA_oB_r\ldots$ sequence, for example, has its $00l$ reflections ($l = 2n$) at the same position as the $00l$ reflections ($l = 3n$) of the rhombohedral struc-

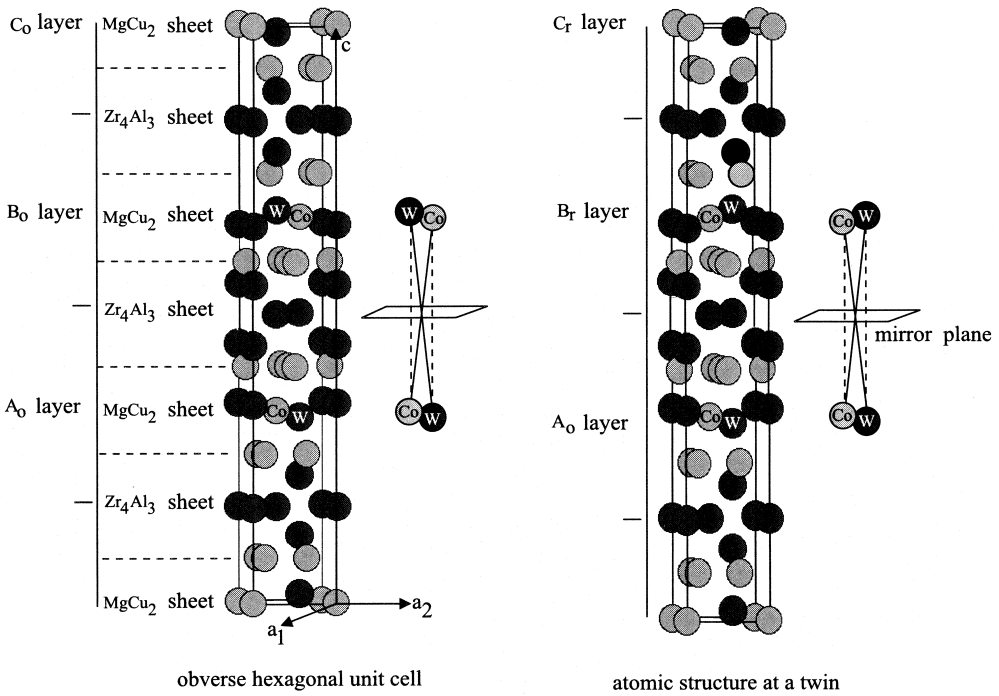

Fig. 3. Unit cell of the μ-phase and atomic structure at a twin.

ture. Hence, diffraction patterns of a twinned μ-phase exhibit isolated spots at $h-k=3n$ (referred to the rhombohedral cells). On the other hand, the $h-k=3n\pm1$ rows consist of linear arrays of closely spaced satellite spots, whose separation is inversely proportional to the lattice parameter c of the structure generated. Continuous streaking instead of distinctive satellite spots results in the case of random twinning.

The Co_7W_6 crystals were found to be considerably disordered. The streaks along c^* (Fig. 1) result from substantial variation in the width of the twinned regions and reflect the random nature of twinning. No tendency to form local sequences was observed in high-resolution images and no fine structure was detected in the streaks (which would indicate the presence of long periods). As it can be seen in Fig. 1(b), the intensity varies considerably along the rows of satellite spots, reaching maxima in the vicinity of the positions of the two basic structures (the obverse and reverse rhombohedral forms). This is in agreement with the interpretation of diffraction patterns of mixed layer compounds and interface modulated structures proposed by Amelinckx and co-workers [18, 19]. As pointed out before for the Fe_7W_6 [20] version of the phase, the random nature of twinning can explain the existence of $1\bar{1}0$ and $2\bar{2}0$ extinction reflections observed in [001] diffraction patterns (Fig. 4). In fact, the distribution in the diffraction space is such that many reciprocal streaks parallel to the c^*-direction are arranged in a hexagonal lattice. The intersection of the Ewald sphere with these streaks causes intensity to appear at forbidden reflection sites.

The deliberate specimen tilt of 10 mrad around the $[1\bar{1}0]$ axis enhanced the contrast difference between adjacent twin domains for observations along the [110] zone axis (see Fig. 2). This eased the task of evaluating the size distribution of the twin domains. A high twin density of 3.9×10^8/m was obtained from measurements performed along 24 μm of the modulation direction. The average number of layers (see Fig. 3) in a twin domain being 3.01, with a large standard deviation of 1.77. Since the measurements were carried out on several different film negatives, it was not possible to directly assess the overall obverse/reverse proportion owing to contrast reversal. Nevertheless, the values measured in every case suggested equipartition. Figure 5 presents the experimental frequency distribution of the twin domain size. The size distribution is peaked at one and follows a statistical distribution based on a 0.33 twinning probability at each possible mirror plane of the μ-phase structure. As an example, sequences corresponding to twinning at three consecutive possible mirror planes ($A_oB_rA_oB_r$) have an expected proportion among general four layer groups of 0.06.

The high twinning probability points to a rather low energy increase associated with the mirror operation. The similarity in atomic arrangement between the defect region and the perfect crystal seems to be responsible for this behaviour and the *ab initio* calculation results presented in Section 3.3 clearly confirm this expectation. The mirroring mistake is closely related to the structure building principle and the massive twinning observed suggests a layer-by-layer growth process with a ledge propagation mechanism. Each layer at the solid–liquid interface having the possibility to grow with an obverse or reverse orientation. This appears to be an intrinsic feature of the μ-phase, because to our knowledge μ-phase crystals free of this type of defect have never been observed [6, 8, 10–12, 21].

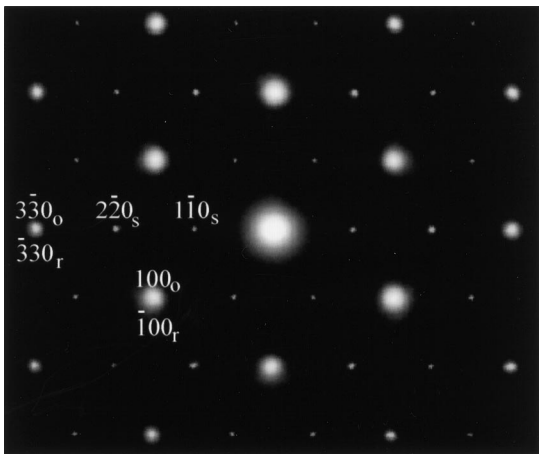

Fig. 4. Diffraction pattern of Co_7W_6 along the [001] zone axis presenting intensity at the μ-phase lattice extinction spots $1\bar{1}0$ and $2\bar{2}0$. Subscripts o stand for the obverse form of the rhombohedral cell, r for the reverse and s for streaking.

3.2. Image simulation

Figure 6 presents a high-resolution image of the Co_7W_6 μ-phase, obtained with axial [110] illumination. The objective aperture used allowed diffracted beams up to $3\bar{3}0$. A twin is indicated and the insets show the result of image simulation optimizations. Cross-correlation factors of 0.662 and 0.635 were achieved for, respectively, the bulk and twin region. The parameter values obtained after 100 generations can be found in Table 2. The experimental reference images, the optimized simulations with the real simulated contrast and the atomic structure superposition can be seen in Fig. 7. Evaluation of the indvidual effects of crystal tilt, beam tilt and achromatic damping enables us to conclude that the shift of the contrast maxima relative to the atomic column positions [Fig. 7(c)] is mainly due to beam tilt. Beam tilt could be expected since a voltage-centre alignment (and not a coma-free alignment) was performed before obtaining the experimental images.

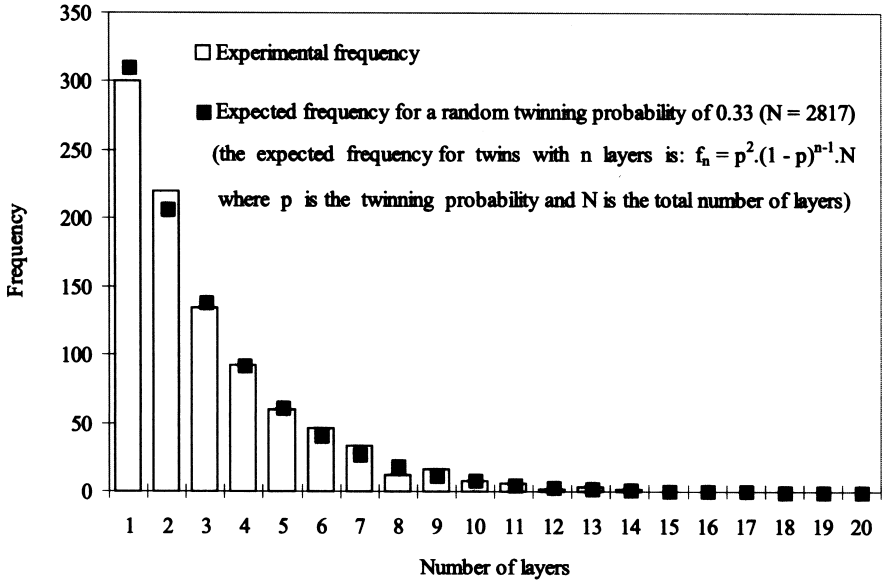

Fig. 5. Size distribution of the twin domains in typical Co_7W_6 grains. The measurements were performed on a population of 935 twins. Since the total number of layers distributed over the twin population was 2817, the twinning probability at each potential mirror plane of the μ-phase structure is 0.33. The experimental frequencies agree with a statistical distribution based on a 0.33 twinning probability, assuming an equipartition of the obverse/reverse forms.

In a quantitative match it is possible to compare image average intensity (on a scale where the incident intensity is one), image contrast (which can be defined as the standard deviation of the intensity) and image pattern [22, 23]. In the present case, because no intensity calibration was performed and the grey scale of the experimental images was adjusted, only pattern matching could be evaluated. The cross-correlation factor is defined as

$$\mathrm{xcf}(I_{\mathrm{exp}}, I_{\mathrm{sim}}) = \frac{\sum (I_{\mathrm{exp},jk} - \overline{I_{\mathrm{exp}}})(I_{\mathrm{sim},jk} - \overline{I_{\mathrm{sim}}})}{\sqrt{\sum (I_{\mathrm{exp},jk} - \overline{I_{\mathrm{exp}}})^2 (I_{\mathrm{sim},jk} - \overline{I_{\mathrm{sim}}})^2}}$$

where $I_{\mathrm{exp},jk}$ and $I_{\mathrm{sim},jk}$ are the intensity of the pixels situated at (j, k) in the experimental and simulated images, respectively, and $\overline{I_{\mathrm{exp}}}$ and $\overline{I_{\mathrm{sim}}}$ are the average values of intensity in the two images. Due to the normalizing property of the denominator, the xcf is not sensitive to mean intensity or overall contrast variance, being in fact a pattern-correlation factor.

The large number of parameters involved in modelling the actual performance of the microscope lens undermines confidence in the uniqueness of this type of fits. It is therefore usually pointed out that no single value obtained from such optimizations should be believed to be an exact solution [24, 25]. Nevertheless, a considerable degree of consistency exists in the values resulting from the two optimization processes (Table 2), which should be strictly expected for microscope related parameters. In fact, during the optimization of the defect region (initialized with the bulk optimum parameters) beam tilt

Table 2. Parameters obtained with IDIM and a simulated evolution optimization strategy [13]

	Bulk	Twin initialized with the optimum bulk parameters
Number of atoms	117	78
Defocus (nm)	5.1	6.5
Thickness (nm)	4.0	4.1
Beam tilt [00$\bar{1}$] (mrad)	1.0	0.9
Beam tilt [1$\bar{1}$0] (mrad)	−0.4	−0.4
Crystal tilt [001] (mrad)	0.4	0.2
Crystal tilt [1$\bar{1}$0] (mrad)	−0.7	−0.5
Mtf[a] [00$\bar{1}$] (nm)	0.04	0.05
Mtf[a] [1$\bar{1}$0] (nm)	0.01	0.03
xcf	0.662	0.635

[a] Variables of an anisotropic modulation transfer function, named as achromatic damping envelope. This function is an elliptical Gaussian and the variables are relative to two given preferential directions. Achromatic damping covers the effect of the modulation transfer of the film and scan-camera and also includes specimen vibration, drift and other damping effects affecting the scattering factors like amorphous layers [24, 25].

values were remarkably stable throughout the evolution. The differences between the two experimental regions (Fig. 6) correspond to small variations in thickness, crystal tilt and defocus (due to a possible inclination and/or thickness difference), as well as in the proportion of the amorphous layers. However, that the simulation process could account for those contributions independently is doubtful. More than any residual displacements at the interface, local fluctuations in the quality of the experimental images and the existence of a second defect in the supercell seem to have caused a worse match for the twin. The low values of cross-correlation factor hindered any attempt to deduce information about atom displacements at the defect from the analysis of the experimental high-resolution image. The simulations enabled none the less the approximate position of the atomic columns to be established and allowed a positive identification of the defect location.

To check whether the optimization would converge to the same values, another run was carried out for the twin image from different initial conditions. The results are shown in Table 3. Although the values achieved are close to the ones obtained previously (especially for thickness and beam tilt), the xcf obtained (0.639) indicates that IDIM was not able to find the global optimum for the twin image when initialized with the optimized bulk parameters (xcf = 0.635). Escape from the local opti-

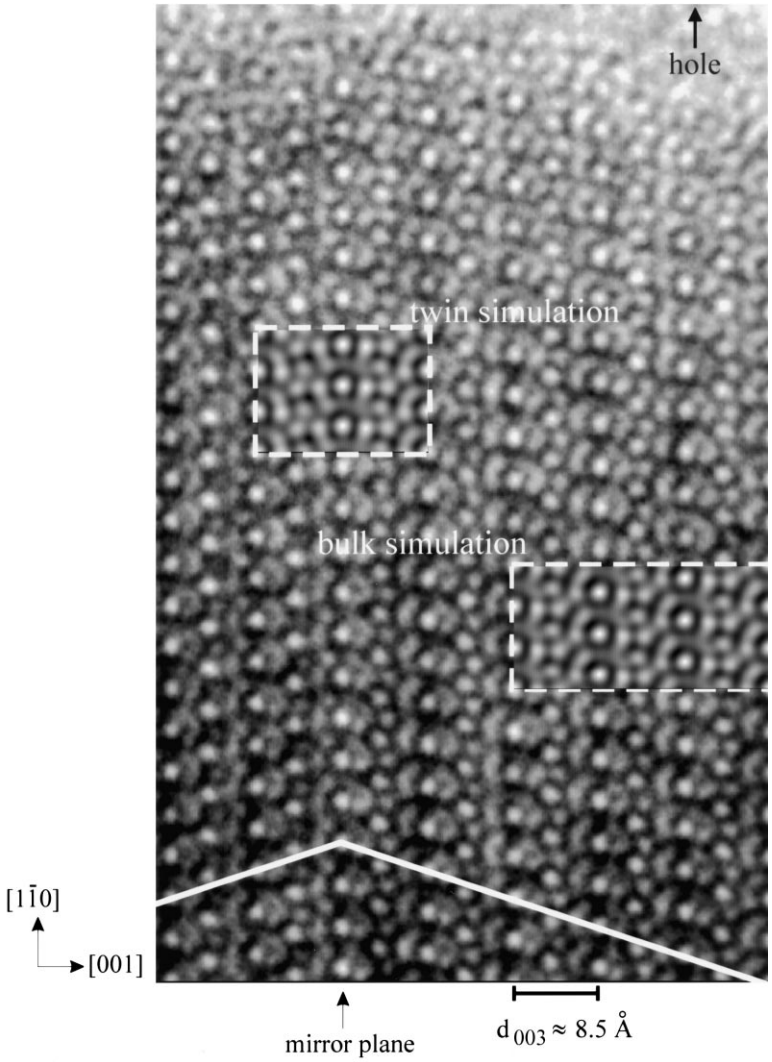

Fig. 6. HRTEM picture of the Co_7W_6 phase taken along the [110] zone axis. A twin is indicated. Insets with optimized image simulations are shown at the locations where the reference images were taken from. The contrast of the simulated images was changed for a better visual match. The experimental reference images, the real simulated contrast and the atomic structure superposition are presented in Fig. 7. The cross-correlation factors (xcf) between the simulated and the experimental images were 0.662 and 0.635, for the bulk and twin cases, respectively. The optimization parameters can be found in Table 2.

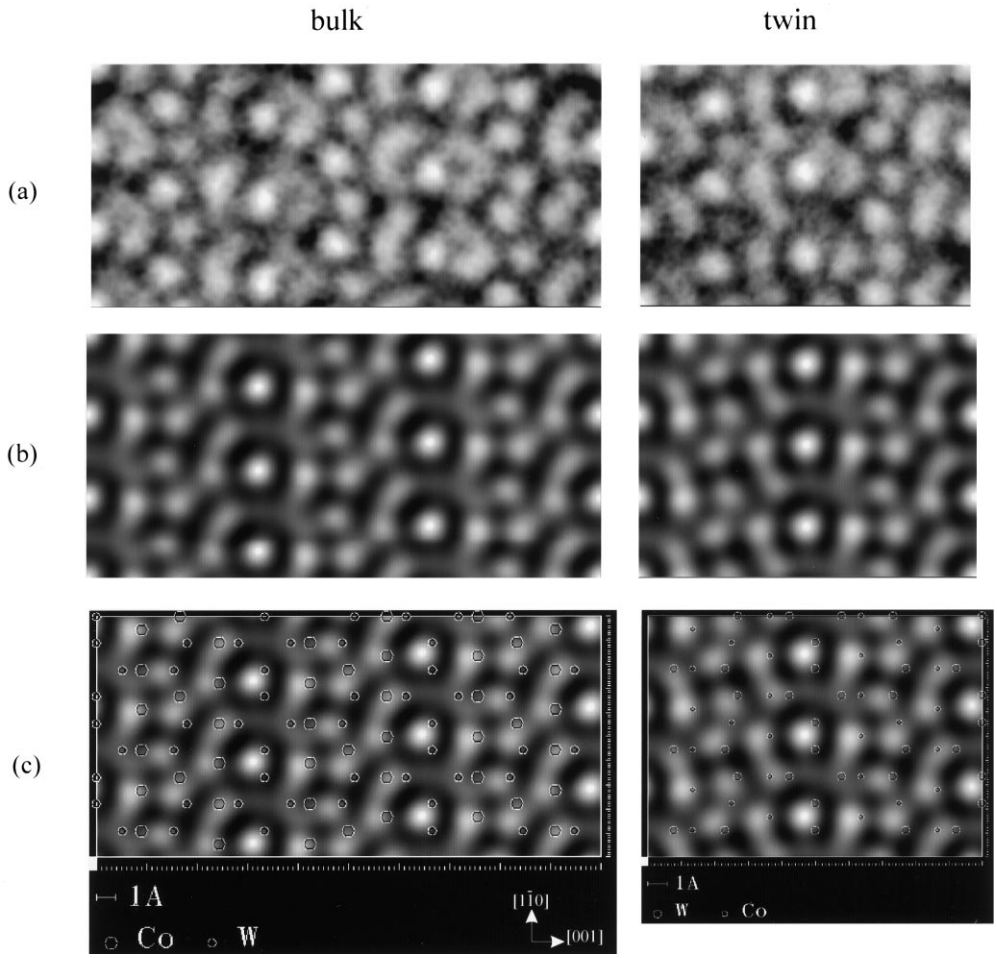

Fig. 7. HRTEM images of the bulk and defect structure along the [110] zone axis: (a) experimental references; (b) optimized simulations after lateral positioning; (c) optimized simulations with atomic structure superposition before lateral positioning. The brightest regions correspond to pairs of W atomic columns situated at the middle of the Zr_4Al_3 sheets (compare with the middle planes in Fig. 3). Cross-correlation factors of 0.662 and 0.635 were obtained for the bulk and twin case, respectively. The optimized parameters used in the image simulations can be found in Table 2.

mum might however have been ruled out by a too restrictive number of generations (interrupt criterion used). Nevertheless, the slightly better xcf produced in the independent twin simulation was obtained at the cost of higher achromatic damping values and seems therefore less reliable.

Since the μ-phase imaged corresponds a higher Co content (56.7 at.% [2]) than the stoichiometric composition (53.8 at.%), a new supercell was defined in which all the W sites were set to have 0.06 of Co occupancy. The results obtained with such a supercell are also presented in Table 3. The

Table 3. Parameters obtained in different ways of fitting

Number of atoms	Twin independent initialization 78	Bulk 6% Co occupancy of W sites 171
Defocus (nm)	7.5	5.9
Thickness (nm)	4.1	3.3
Beam tilt [001] (mrad)	1.0	1.1
Beam tilt [1$\bar{1}$0] (mrad)	−0.8	−0.3
Crystal tilt [001] (mrad)	1.0	−0.1
Crystal tilt [1$\bar{1}$0] (mrad)	−1.0	−1.2
Mtf[a] [001] (nm)	0.06	0.05
Mtf[a] [1$\bar{1}$0] (nm)	0.05	0.01
xcf	0.639	0.659

[a] See footnote to Table 2.

thickness converged to a significantly different value indicating that the process was sensitive to the change. However, the typically low xcf value shows that the lack of agreement does not have origin in this type of chemical differences. For a specimen thickness below 10 nm, any contribution of absorption to the image can be expected to have a minor contribution. The effect of the Debye–Waller factor (DWF), on the other hand, has been found not to be so negligible (Fanidis in Ref. [26]). Although with the risk of overestimating the importance of these parameters, optimization runs were performed using absorption and DWF as single variables (after optimization of the other parameters). The agreement showed however no significant improvement.

The treatment of the image formation in the microscope was performed using the weak-phase-object approximation (WPOA), which in the case of crystals containing heavy atoms (such as W) is considered not to hold for thickness higher than 0.5 to 1 nm [27]. The low xcf values obtained (when compared, for example, with the ones achieved for simple metal cases and even ceramics like sapphire [25]) confirm this approximation to be an oversimplified description of the electron–object interaction in the case of the specimen studied. However, as it can be seen in Fig. 6, the qualitative pattern resemblance between the simulated and experimental images is rather good. Hence, although the contrast transfer function of the microscope lens does not seem to be well modelled using conventional simulations, here we have demonstrated that a quantitative image assessment can be used to efficiently retrieve approximated imaging conditions for complex phases with heavy atoms. The aim was to provide the best fit that could be generated with the existing simulation programs.

3.3. Energy considerations

The results obtained from the *ab initio* calculations are presented in Table 4. Since the hexagonal cell of the perfect μ-phase corresponds to an $A_oB_oC_o$ layer stacking and the defect hexagonal cell corresponds to an A_oB_r stacking (see Fig. 3), the unit chosen for energy comparisons was the layer (seven Co atoms and six W atoms). The relaxation processes carried out did not converge to the experimental lattice parameters and the expansion observed points to a missing attractor term in the pseudopotentials used. However, this was not considered critical for an energy difference assessment. According to the calculations, twinning on every possible mirror plane induces a volume contraction of 3%. As expected, a quite low energy of about 6.4×10^{-22}J/atom is involved in the planar defect. The largest changes in atomic position correspond to the atoms labelled in Fig. 3, being 0.011 and 0.007 nm for Co and W, respectively. It should be noted, however, that due to the two consecutive planar defects contained in the $P6_3/mmc$ supercell, the distortion induced by one mirror operation may have been somewhat accommodated by the next one.

Because the obverse/reverse variants are energetically equivalent, the present situation seems to correspond to polytypism. Structurally, polytypism may in fact be regarded as a special case of polymorphism, where the structure varies in only one dimension. As polytypes are composed of virtually identical units, the free-energy differences are small and the kinetics of solid-state transformations between them are often sluggish. Hence, it is difficult to establish experimentally whether these type of systems are truly in equilibrium. Nevertheless, at least some polytypes have already been shown to possess thermodynamically definable fields of stability [28–30]. It was earlier realized that nearest-neighbour interactions alone could not account for the general variety of polytypes. However, the addition of a second competing interaction opens up a great wealth of stacking sequences. For this reason a statistical mechanical model like the axial next-nearest-neighbour Ising (ANNNI) model is often used to explain polytypic behaviour [31–35]. In these Ising-model based approaches, polytypism is considered to be (at least partly) an equilibrium phenomenon, and the relative stability of long stacking sequences is justified in terms of a subtle balance between enthalpy and entropy (resulting from short-range competing interactions between the polytypic units). In an ANNNI type of analysis of the μ-phase behaviour, the obverse/reverse configurations would be taken as the pseudo-spins. In the present situation, the 0.33 twinning probability indicates that the μ-phase was formed under conditions of preference for first nearest-neighbours

Table 4. Results obtained from the *ab initio* calculations for the perfect μ-phase cell ($R\bar{3}m$) and defect cell ($P6_3/mmc$)

		Co (at.%)	a_r (nm)	α_r (deg)	a_h (nm)	c_h (nm)	Energy (10^{-15} J/unit cell)	Energy (10^{-15} J/Co_7W_6)
$R\bar{3}m$ (13 atoms)	Co rich (experimental)	56.7 [2]	0.892 [3]	30.70 [3]	0.472 [3]	2.548 [3]	–	–
	W rich (experimental)	51.5 [2]	0.899 [3]	30.67 [3]	0.475 [3]	2.567 [3]	–	–
	Stoichiometric (non-relaxed)	53.8	0.896[a]	30.69[a]	0.474[a]	2.559[a]	−1.10123	−1.10123
	Stoichiometric (relaxed)	53.8	0.917	30.68	0.485	2.619	−1.10142	−1.10142
$P6_3/mmc$ (26 atoms)	Stoichiometric (relaxed)	53.8	–	–	0.487	1.726	−2.20280	−1.10141

[a] Interpolated from the experimental values.

with the same spin, that is under $J_1/J_2 < -2$ conditions. However, the apparent equipartition of the obverse/reverse forms suggests that the phase was generated in a pseudo-paramagnetic domain of stability, where the preference for first-neighbours with the same spin just reflects short-range order. In this case, the competition with second nearest-neighbour interactions might not be necessary to explain the behaviour of the μ-phase. The entropic term based only on first-neighbour configurations may suffice and a simple Ising model can be used to describe the observations. In fact, due to the large distances involved (a unit is 8.5 nm wide) it is reasonable to assume a minor role of second nearest-neighbour interactions. Following this discussion it could be expected that under different conditions (lower temperatures or different compositions) the μ-phase would tend to a pseudo-ferromagnetic structure. In general, the earlier work carried out on the μ-phase did not present any assessment on the obverse/reverse relation, however, in one case an obverse proportion of more than 0.95 was determined [21], clearly pointing to a pseudo-ferromagnetic behaviour.

4. CONCLUSIONS

- The Co_7W_6 μ-phase exhibits a high density of sub-unit cell twins, where the interfaces are pure mirror planes.
- The size of the twin domains in typical Co_7W_6 grains was found to follow a statistic distribution based on a 0.33 twinning probability at each possible mirror plane.
- A rather low energy is involved in the mirror operation, as derived from *ab initio* calculations, which explains the massive twinning observed.
- The potential of quantitative HRTEM image simulation was demonstrated for a complex perfect and defect structure involving heavy atoms.

Acknowledgements—The work described in this paper was partly supported by the Portuguese Foundation for Science and Technology (financed by the Science and Technology Sub-programme of the European Community second framework programme).

REFERENCES

1. Spence, J. C. H., *Experimental High Resolution Electron Microscopy*. Oxford University Press, New York, 1988.
2. Naidu, S. V., Sriramamurthy, A. M. and Rao, P. R., *J. Alloy Phase Diagrams*, 1986, **2**, 43.
3. Magneli, A. and Westgren, A., *Z. anorg. Chem.*, 1938, **238**, 268.
4. Forsyth, J. B. and D'Alte da Veiga, L. M., *Acta crystallogr.*, 1962, **15**, 543.
5. Andersson, S., *J. Solid St. Chem.*, 1978, **23**, 191.
6. Stenberg, L. and Andersson, S., *J. Solid St. Chem.*, 1979, **28**, 269.
7. Ishimasa, T., Kitano, Y. and Komura, Y., *Physica status solidi (a)*, 1981, **66**, 703.
8. Stenberg, L., *Chem. Scripta*, 1978–79, **14**, 219.
9. Stenberg, L., *Acta crystallogr.*, 1979, **A35**, 387.
10. Zhu, J. and Ye, H. Q., *Scripta metall. mater.*, 1990, **24**, 1861.
11. Forsyth, J. B. and d'Alte da Veiga, L. M., *Acta crystallogr.*, 1962, **15**, 543.
12. Hiraga, K., Yamamoto, T. and Hirabayashi, M., *Trans. Japan Inst. Metals*, 1983, **24**, 421.
13. Möbus, G. G., Schweinfest, R., Gemming, T., Wagner, T. and Rühle, M., *J. Microsc.*, 1998, **190**, 109.
14. Stadelmann, P., *Ultramicroscopy*, 1987, **21**, 131.
15. Payne, M. C., Teter, M. P., Allen, D. C., Arias, T. A. and Joannopoulos, J. D., *Rev. mod. Phys.*, 1992, **64**, 1045.
16. Molecular Simulations Inc., San Diego, 1997.
17. Kleinman, L. and Bylander, D. M., *Phys. Rev. Lett.*, 1982, **48**, 1425.
18. Van Tendeloo, G., Van Dyck, D., Kuipers, S. and Amelinckx, S., *Physica status solidi (a)*, 1987, **101**, 339.
19. Van Tendeloo, G., Van Dyck, D., Kuipers, S., Zandbergen, H. W. and Amelinckx, S., *Physica status solidi (a)*, 1987, **102**, 597.
20. Zhu, J. and Ye, H. Q., *Scripta metall. mater.*, 1990, **24**, 1861.
21. Wagner, V., Conrad, M. and Harbrecht, B., *Acta crystallogr.*, 1995, **C51**, 1241.
22. Hÿtch, M. J. and Stoobs, W. M., *Ultramicroscopy*, 1994, **53**, 191.
23. Boothroyd, C. B., *J. Microsc.*, 1998, **190**, 99.
24. Möbus, G., *Ultramicroscopy*, 1996, **65**, 205.
25. Möbus, G. and Dehm, G., *Ultramicroscopy*, 1996, **65**, 217.
26. Krakow, W. and O'Keefe, M., *Computer Simulation of Electron Microscope Diffraction and Images*. The Minerals, Metals and Materials Society, Warrendale, PA, 1989.
27. Buseck, P., Cowley, J. and Eyring, L., in *High-Resolution Transmission Electron Microscopy and Associated Techniques*. Oxford University Press, Oxford, 1992, p. 78.
28. Jepps, N. W. and Page, T. F., *Polytype Structures*, ed. P. Krishna. Pergamon Press, Oxford, 1983, p. 259.
29. Akaogi, M., Akimoto, S., Horioka, K., Takahashi, K. and Horiush, H., *J. Solid St. Chem.*, 1982, **44**, 257.
30. Stel'makh, S., Paloz, B. and Gierlotka, S., *Mater. Sci. Forum*, 1996, **228–231**, 663.
31. Price, G. D. and Yeomans, J., *Acta crystallogr.*, 1984, **B40**, 448.
32. Price, G. D., Parker, S. C. and Yeomans, J., *Acta crystallogr.*, 1985, **B41**, 231.
33. Angel, R. J., Price, G. D. and Yeomans, J., *Acta crystallogr.*, 1985, **B41**, 310.
34. Kaburagi, M. and de Fontaine, D., *Springer Series in Solid-State Sciences*, 1993, **114**, 157.
35. Baronnet, A., *Rev. Mineral.*, 1992, **27**, 230.